AEROSPACE RESEARCH COMMUNICATIONS
ORIGINAL RESEARCH
published: 25 March 2026
doi: 10.3389/arc.2026.16179

Study on the Influence of Distributed Propeller Slipstream Effects Considering Lift-Enhancing Characteristics

Ziqi Lan, Min Zhong, Yue Xu, Yuhang Wang, Haitao Zhu and Yan Li*

Chinese Aeronautical Establishment, Beijing, China

This study investigates the slipstream effect generated by a distributed propeller configuration on an aircraft designed for lift enhancement. A numerical simulation approach adopting the Multiple Reference Frame (MRF) method is implemented to assess the influence of key propeller parameters, such as disc diameter and rotational speed, on the slipstream. A specific distributed propeller layout aimed at enhancing lift is proposed and examined. The aerodynamic interference caused by the propeller slipstream on the full aircraft is systematically studied, with a focus on its impact on overall aerodynamic characteristics. The results indicate that the slipstream effect is highly sensitive to variations in propeller disc diameter and rotational speed. Specifically, increasing the rotational speed or reducing the disc radius intensifies the slipstream. However, higher speeds may lead to challenges in power requirements and motor compatibility. For the distributed layout, the propeller flow not only accelerates the wake but also interacts with the wing, leading to segmentation and a reorganization of the vortex structure. This interaction drastically alters the pressure distribution over the wing surface. Consequently, both the lift and drag coefficients increase under slipstream conditions. Furthermore, the slipstream's induced flow delays boundary layer separation at key areas, resulting in improved stall characteristics.

Keywords: aerodynamic characteristic, distributed propeller, multiple reference frame, numerical simulation, slipstream effect

OPEN ACCESS

Correspondence
Ziqi Lan,
2422078701@qq.com

Received: *03 January 2026*
Revised: *25 February 2026*
Accepted: *10 March 2026*
Published: *25 March 2026*

Citation:
Lan Z, Zhong M, Xu Y, Wang Y, Zhu H and Li Y (2026) Study on the Influence of Distributed Propeller Slipstream Effects Considering Lift-Enhancing Characteristics. Aerosp. Res. Commun. 4:16179. doi: 10.3389/arc.2026.16179

INTRODUCTION

Green aviation research is crucial for addressing global challenges such as climate change, environmental pollution, and resource scarcity, and is integral to achieving sustainable development within the aviation industry [1–4]. Aircraft powered by Distributed Electric Propulsion (DEP) systems, which utilize electrically driven multiple propellers, represent a promising direction in this field [5–7]. DEP technology offers potential benefits including enhanced aerodynamic efficiency, increased payload capacity, improved fuel efficiency, and greater operational robustness. Consequently, it has emerged as a focal area in green aviation research and is often cited as a potentially transformative technology for future aviation [8].

Aircraft with distributed electric or hybrid propellers not only achieve high propulsion efficiency but also fully utilize the propeller slipstream. Such a configuration enables a favorable aerodynamic coupling between the electric propulsion system and the wing, thus significantly improving the

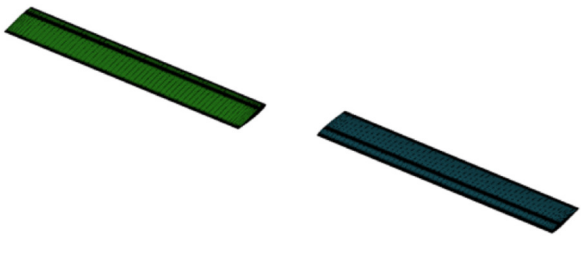

FIGURE 1 | C-T rotor model.

overall aerodynamic performance of the aircraft. In addition to enhancing lift during takeoff and landing, it can reduce fuel consumption and emissions [9]. Therefore, it has become a new research hotspot in the aviation field worldwide [10–14].

Research on distributed electric propulsion (DEP) aircraft has been advanced significantly by NASA since around 2014. This systematic effort has established key test platforms, including a propeller electric propulsion test rig and the Hybrid-Electric Integrated Systems Testbed (HEIST) [15, 16]. It has also yielded two major technological application pathways: Leading-Edge Asynchronous Propeller Technology (LEAPTech) and the Scalable Convergent Electric Propulsion Technology and Operations Research (SCEPTOR) project. These initiatives have culminated in the development and testing of several DEP aircraft demonstrators, such as the GL-10 [12, 17–19] and the X-57 Mx [20, 21].

The coupled aerodynamic characteristics of blades and wings on Distributed Electric Propulsion (DEP) aircraft are primarily investigated via Computational Fluid Dynamics (CFD) and wind tunnel testing. Early foundational work includes the study by Stoll and Bevirt [22], who in 2014 employed theoretical and CFD analysis to explore wing and propeller integration design. Their results demonstrated the superior efficiency and significant noise reduction potential of DEP aircraft compared to conventional configurations, and they proposed a preliminary concept for a flight test vehicle. In 2016, Stoll's team further conducted a design study for a DEP commuter aircraft [23]. They evaluated various propeller layouts and selected a distributed electric propulsion configuration optimized for high lift. This design was shown to incur less power loss for lift generation compared to a conventional layout, allowing the saved power to be allocated to increase cruise speed, thereby highlighting the potential of DEP configurations for efficient high-speed flight.

Concurrently, advancements have been made in developing lower-order numerical tools for rapid analysis. Patterson and German [24] applied a lifting-line method to simulate the coupled aerodynamics of two- and four-propeller configurations. To efficiently account for propeller-wing interactions, Pavel et al. [25] developed a tool combining blade element momentum theory with a nonlinear lifting-line method. Marcus et al. [26] created a low-order tool based on blade element theory, a panel method, and a propeller model incorporating wing-induced velocities to analyze a propeller mounted on a flapped wing, achieving good agreement with wind tunnel data. Further simplifying the process, Bohari et al. [27, 28] proposed both linear and nonlinear low-order numerical methods that also showed favorable correlation with experimental data.

Research in this field started relatively late in China. Studies on the aerodynamic/propulsion coupling characteristics of distributed electric propulsion aircraft are mainly based on the CFD method. YANG Xiaochuan et al. [29, 30] investigated the wing slipstream effects induced by four different distributed propeller rotation combinations, using a distributed propeller transport aircraft as the research background. They adopted the Reynolds-averaged Navier–Stokes (RANS) equations coupled with the Spalart–Allmaras (SA) turbulence model, and simulated the wing slipstream effects using an actuator disk model instead of real distributed propellers. Yang Wei et al. [31] used an equivalent disk to represent the actual propeller, and applied the RANS equations to the optimal design of distributed propeller arrangement. The optimized configuration increases the lift coefficient by 5.6% and reduces drag by 13.9% during takeoff. Wang Kelei et al. [32] investigated the aerodynamic characteristics of three propeller/wing configurations at low Reynolds numbers, based on a solar-powered unmanned aerial vehicle with distributed propellers. They adopted the MRF method combined with hybrid grid technology and a transition model to solve the RANS equations. The propeller slipstream is shown to effectively enhance the wing lift.

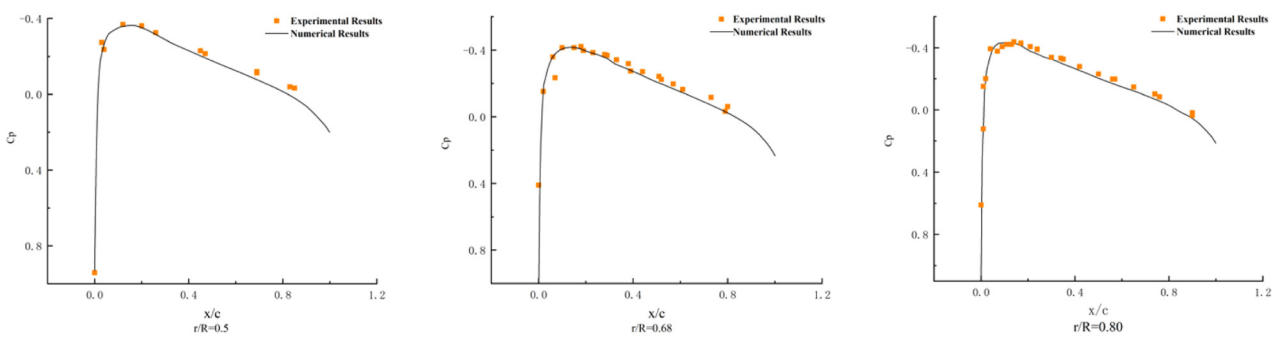

FIGURE 2 | Surface pressure distribution on a C-T rotor in hover.

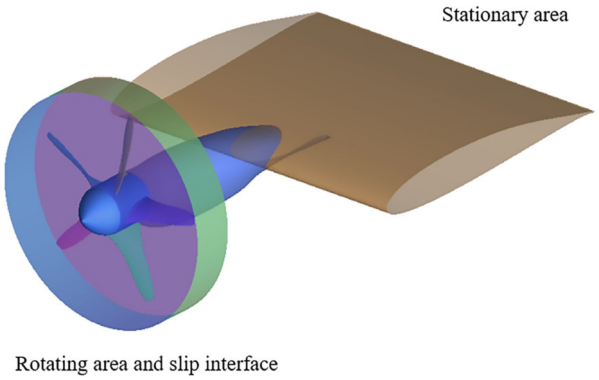

FIGURE 3 | The slip interfaces and computational regions.

Overall, numerical investigations into the aerodynamic/propulsion coupling interference of distributed electric propulsion aircraft are still in the preliminary stage.

This paper investigates a distributed electric propulsion (DEP) aircraft layout optimized for enhanced lift. The MRF method is employed to numerically simulate the slipstream effects of individual propellers under varying key design parameters. The analysis compares the aerodynamic characteristics of the full-configuration aircraft with and without propeller slipstream interaction. Furthermore, a parametric study is conducted to evaluate the influence of different DEP aerodynamic configurations on wing flow fields.

NUMERICAL SIMULATION METHODS AND AERODYNAMIC VALIDATION

MRF Method

For the analysis of propeller slipstream flow fields, extensive computational methods have been developed through long-term research both domestically and internationally. These include the vortex lattice method, the panel method, the actuator disk method, the multiple reference frame method, and the sliding mesh method, among others. The vortex lattice method, the panel method and actuator disk method are characterized by their simplicity and low computational grid requirements. However, the actuator disk method does not account for the rotational effects of the airflow upstream of the propeller, and the specification of blade loading relies heavily on engineering experience and heuristics. Consequently, it is primarily used in the conceptual design and preliminary analysis stages [33–37].

The MRF method and the sliding mesh method are among the most commonly employed approaches for slipstream simulation. The MRF method is a steady-state approximation. In this approach, the grid remains stationary, and the motion of the rotating region is simulated by introducing a rotating reference frame. In contrast, the sliding mesh method is a transient simulation technique that employs an unsteady solver, with the mesh dynamically moving over time. Since MRF assumes a steady flow, it offers higher computational efficiency but cannot accurately capture unsteady flow features. The sliding mesh method provides higher accuracy but demands significantly greater computational resources and time. While results from the sliding mesh method generally agree more closely with

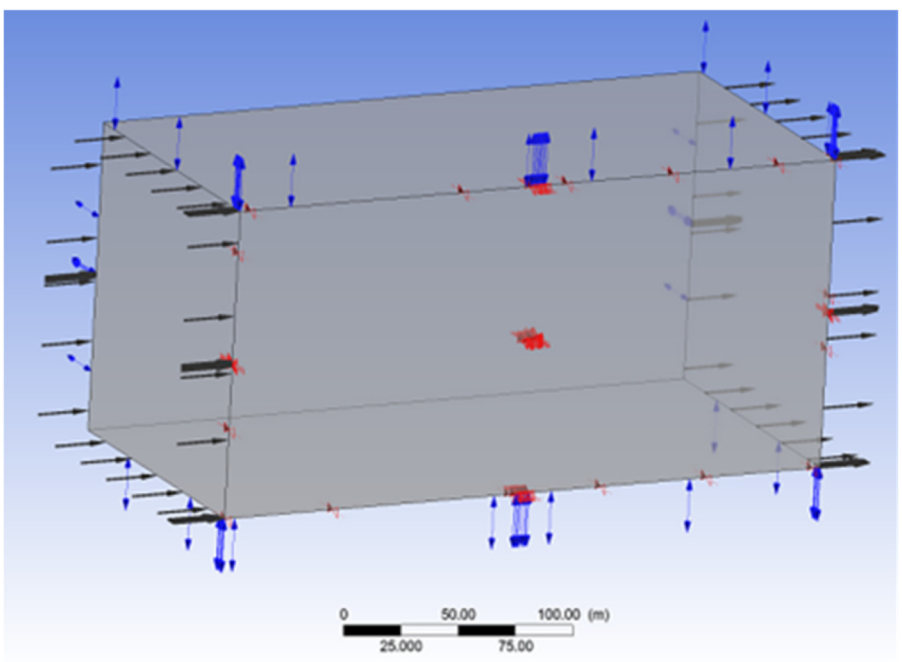

FIGURE 4 | Flow domain and boundary condition.

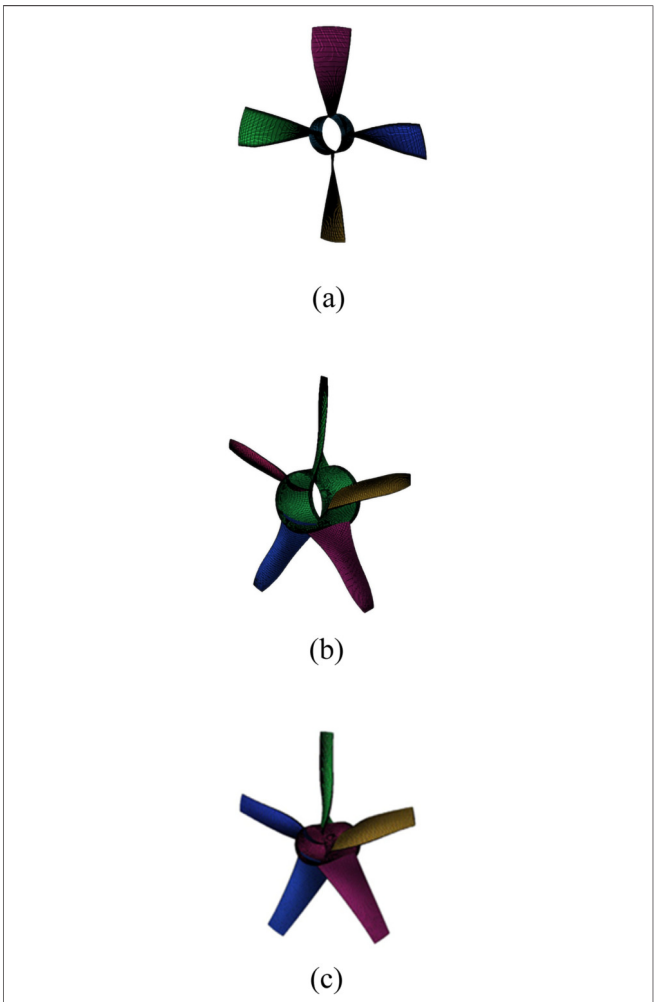

FIGURE 5 | Surface grid structure of propellers with different configurations. **(a)** Four-bladed propeller with a radius of 300 mm. **(b)** Five-bladed propeller with a radius of 285 mm. **(c)** Five-bladed propeller with a radius of 330 mm.

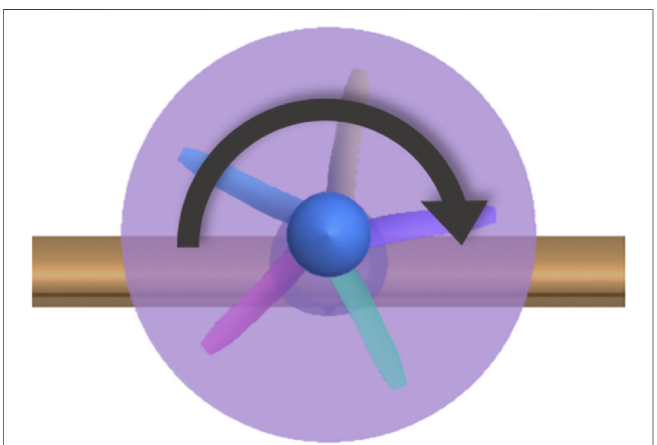

FIGURE 6 | Propeller rotation direction.

experimental data, the MRF method is also capable of capturing the overall flow field variations, and the observed trends are consistent with those obtained using the sliding mesh method. Considering the focus of this study—analyzing the influence of propeller slipstream effects on parameters such as wing/aircraft lift and drag—the MRF method adequately fulfills the research requirements.

Governing Equations

The Reynolds-averaged Navier-Stokes (RANS) equations are solved numerically. For the rotating domain, the equations are formulated in a rotating reference frame. The governing equations in integral form are given in **Equation 1**.

$$\frac{\partial}{\partial t}\iiint_V \mathbf{W}dV + \oiint_{\partial V} \mathbf{H}\cdot\mathbf{n}dS - \oiint_{\partial V} \mathbf{H_v}\cdot\mathbf{n}dS + \iiint_V \mathbf{G}dV = 0 \quad (1)$$

where the definitions of all variables follow those in Ref. [38].

Validation

To validate the accuracy of the MRF method for computing the flow field around rotating bodies, a verification was performed using the measured surface pressure data for the Caradonna-Tung (C-T) rotor published in Reference [39]. The C-T rotor comprises two straight, untwisted blades of constant chord. The airfoil section is the NACA 0012 profile, and the blade radius is 1.143 m. A schematic of the model is shown in **Figure 1**.

The computational setup matched the experimental conditions: a tip Mach number (Mtip) of 0.52, a collective pitch angle (θc) of 0°, and a rotational speed (Ω) of 1,500 rpm.

A comparison between the pressure distributions obtained from the MRF simulation and the experimental data is presented in **Figure 2** for several radial stations: r/R = 0.50, 0.68, 0.80, where c denotes the chord length. As shown in the **Figure 2**, the results calculated using the MRF method exhibit the same trends as the experimental pressure distributions and demonstrate good overall agreement with the test data.

Boundary Conditions and Domain Interfaces

The boundary conditions adopted in the present study include velocity inlet, pressure outlet, no-slip adiabatic wall, and symmetry plane, together with the sliding interface at the junction between the stationary and rotating domains. The sliding interface is modeled using a general mesh interface approach, which ensures the conservation of mass, momentum, and energy fluxes across both sides of the interface.

The cylindrical interface illustrated in **Figure 3** is employed to represent the sliding interface. This cylinder encloses the rotating components of the propeller, namely the blades and the hub. All

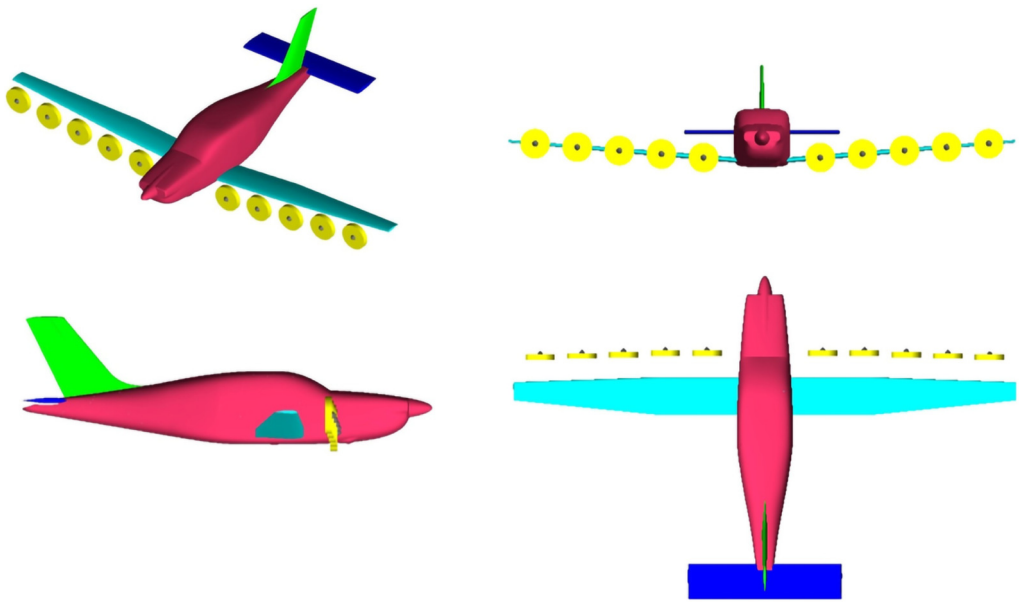

FIGURE 7 | The distributed propellers airplane.

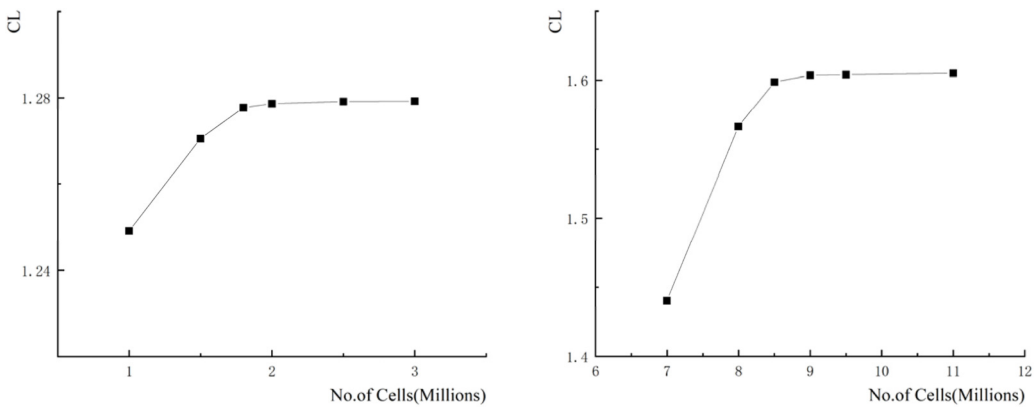

FIGURE 8 | Grid independence study.

regions outside the rotating domain are defined as stationary domains. The interface between the two flow domains is handled via a fluid-fluid coupling scheme.

Figure 4 shows the boundary condition setup. As the inflow velocity is prescribed, the inlet boundary is specified as a velocity inlet with the inflow velocity defined. Solid surfaces such as the propeller blades are set as no-slip walls. The outlet is specified as a pressure outlet with an ambient pressure of 101 kPa and zero pressure gradient, while the far-field open boundary is defined using velocity components.

MODELS AND NUMERICAL SIMULATION

Single Propeller Configuration

Three propeller configurations were selected for analysis, as illustrated in **Figure 5**: a five-bladed propeller with a disk radius of 285 mm, another five-bladed propeller with a 330 mm radius, and a four-bladed propeller with a 300 mm radius. The nacelle connecting the propeller to the wing segment was individually optimized to account for the different hub radii. The rotational direction for all propellers is clockwise when viewed from the upstream direction, as shown in **Figure 6**.

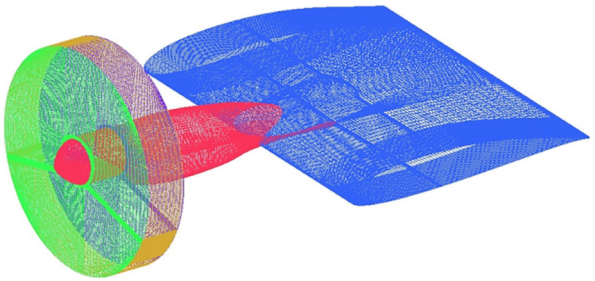

FIGURE 9 | Single propeller and wing surface mesh.

Distributed Propeller Aircraft Configuration

Based on an analysis of the influence of a single propeller's slipstream on the aerodynamic characteristics of a wing section, the optimal propeller configuration was determined. This configuration was subsequently applied to a distributed propeller arrangement to investigate the aerodynamic performance of an aircraft without high-lift devices under low-altitude and low-speed conditions, and to assess the impact of the slipstream on the wing.

To avoid inter-propeller slipstream interference while considering propeller radius and wing span, five propellers were arranged along each wing. All distributed propellers rotate in the same clockwise direction (viewed from upstream) as the single propeller, consistent with **Figure 6**.

The full aircraft model, depicted schematically in **Figure 7**, features a conventional low-wing design with a vertical tail. Key dimensions include a wingspan of 11.9 m, a length of 7.7 m, a height (without landing gear) of 1.38 m, a wing area of 3.46 m^2, and a maximum fuselage width of 1.3 m. To reduce computational cost, a symmetric half-span model was employed for the simulations. The propellers are numbered 1 to 5 from the fuselage side towards the wingtip.

Computational Grid

Structured hexahedral meshes were generated for both the single propeller configuration and the distributed propeller aircraft configuration. For all cases, the rotating components (blades and a portion of the hub) were embedded within a cylindrical

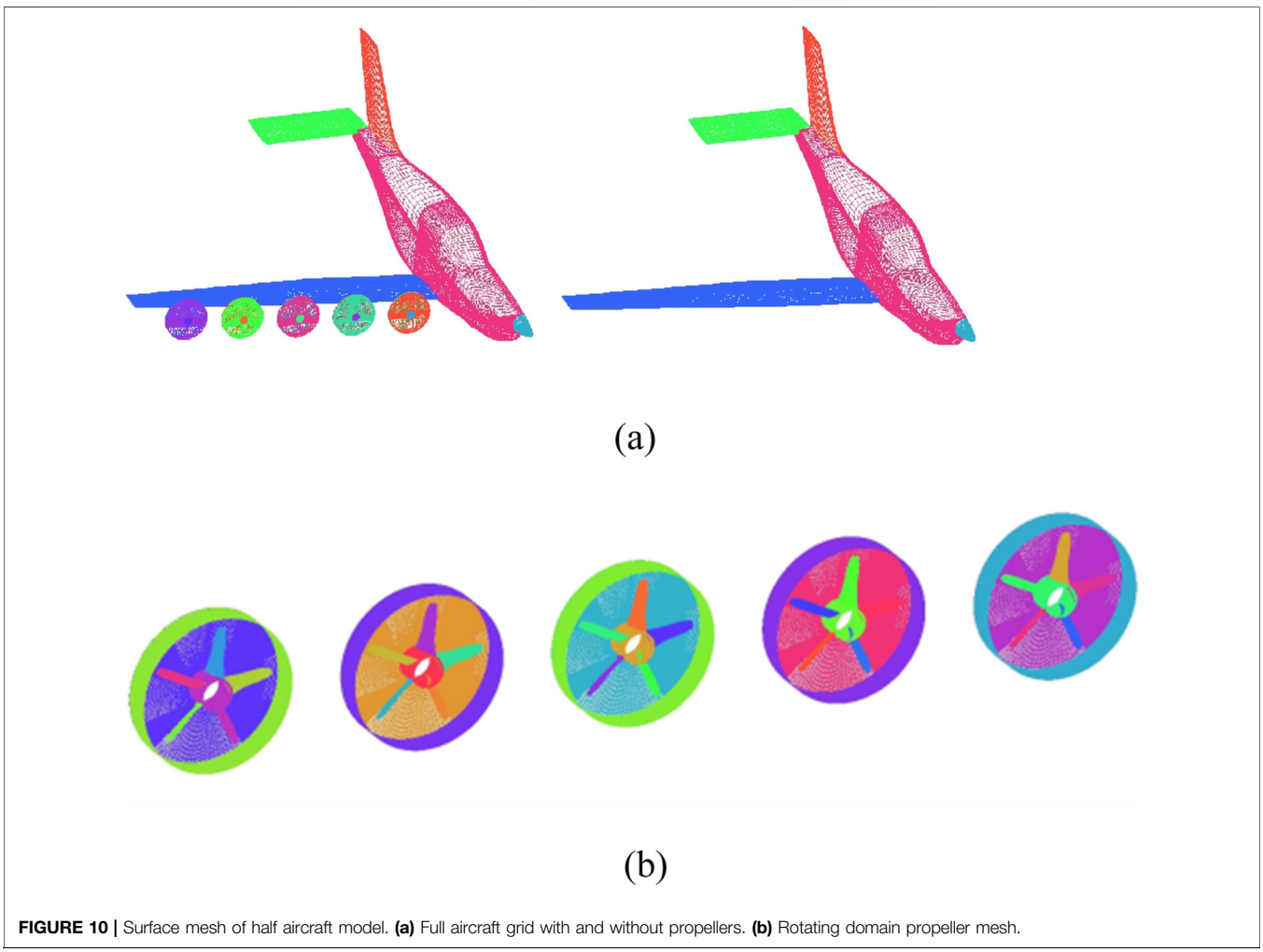

FIGURE 10 | Surface mesh of half aircraft model. **(a)** Full aircraft grid with and without propellers. **(b)** Rotating domain propeller mesh.

TABLE 1 | Test conditions.

Computational Configuration	Free stream velocity (m/s)	Angle of attack (°)	RPM
Single propeller	28/32/34/38	0/2/4/6/8/10	2000/2500/3,000/3500/4,000/4500/5,000
Distributed propellers	33	0/2/4/6/8/10	2000/2500/3,000/3500/4,000/4500/5,000

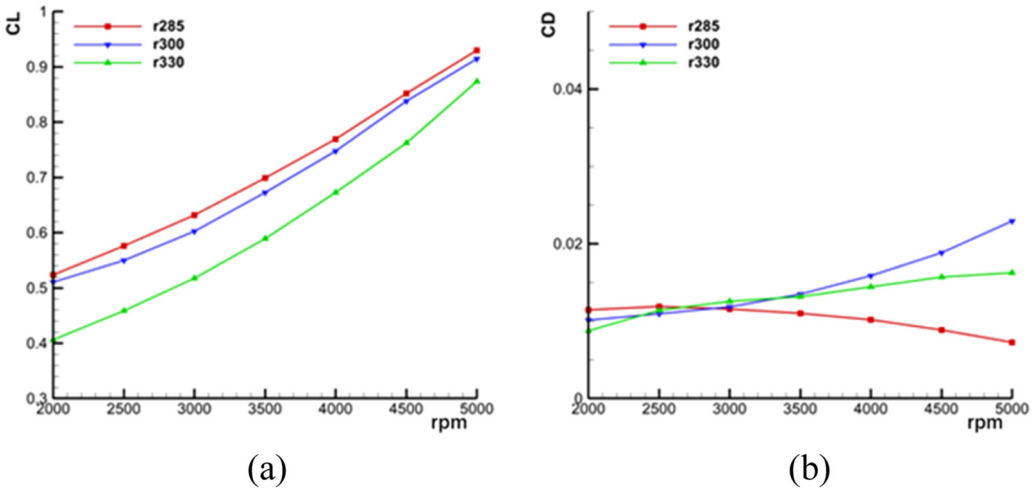

FIGURE 11 | The slipstream effect's impact on the wing section's aerodynamic characteristics at varying propeller speeds. **(a)** Lift coefficient. **(b)** Drag coefficient.

rotational domain, as illustrated in **Figure 3**. To ensure high mesh quality, the computational domain was partitioned into two distinct zones: one encompassing the cylindrical rotational domain around the propeller, and the other covering the remaining stationary fluid region. These zones were connected using an overset (chimera) grid technique.

A grid independence study was performed for both the single propeller and distributed propeller aircraft configurations to ensure the adequacy of the selected mesh resolutions, as shown in **Figure 8**. For the single propeller case, the total mesh size was approximately 2 million cells across both stationary and rotating domains, distributed over 175 blocks, as shown in **Figure 9**. For the half-model simulation of the full aircraft, the mesh consisted of roughly 9 million cells across 1200 blocks, as shown in **Figure 10**. The near-wall mesh was refined to achieve a first-layer cell height satisfying $y^+ \leq 1$. In this full-aircraft simulation, the nacelles were omitted, and each propeller was modeled within its own rotating domain grid. The aircraft geometry was segmented into three main components: wing, fuselage, and tail. Forces and moments on each propeller were monitored individually.

To enable a direct comparison with the baseline configuration without propellers, a separate mesh was generated. This was done by removing the propeller components and their rotational domains from the existing full-aircraft mesh topology while preserving the node distribution and topology in the stationary domain, followed by local re-gridding.

Numerical Cases

To satisfy the power requirements of the propeller motor and account for the aircraft takeoff and landing conditions, a single propeller configuration is investigated at inflow velocities ranging from 28 m/s to 38 m/s, angles of attack from 0° to 10°, and propeller rotational speeds from 2000 rpm to 5,000 rpm.

Based on the numerical results and analysis of the single propeller configuration, an appropriate propeller configuration is selected for the distributed -propeller aircraft. A freestream velocity of 33 m/s is then adopted for the takeoff and landing analysis.

The numerical conditions for both single and distributed propeller configurations are summarized in **Table 1**.

SIMULATION RESULTS

The numerical simulation results obtained using the Moving Reference Frame (MRF) method were analyzed for both the single-propeller configuration and the powered takeoff and landing configuration. The analysis primarily focused on the aerodynamic force characteristics of the wing section and the complete aircraft, as well as the variations in the velocity and pressure fields. Parameters specifically related to the propeller, such as thrust and propulsive efficiency, were not within the scope of this study.

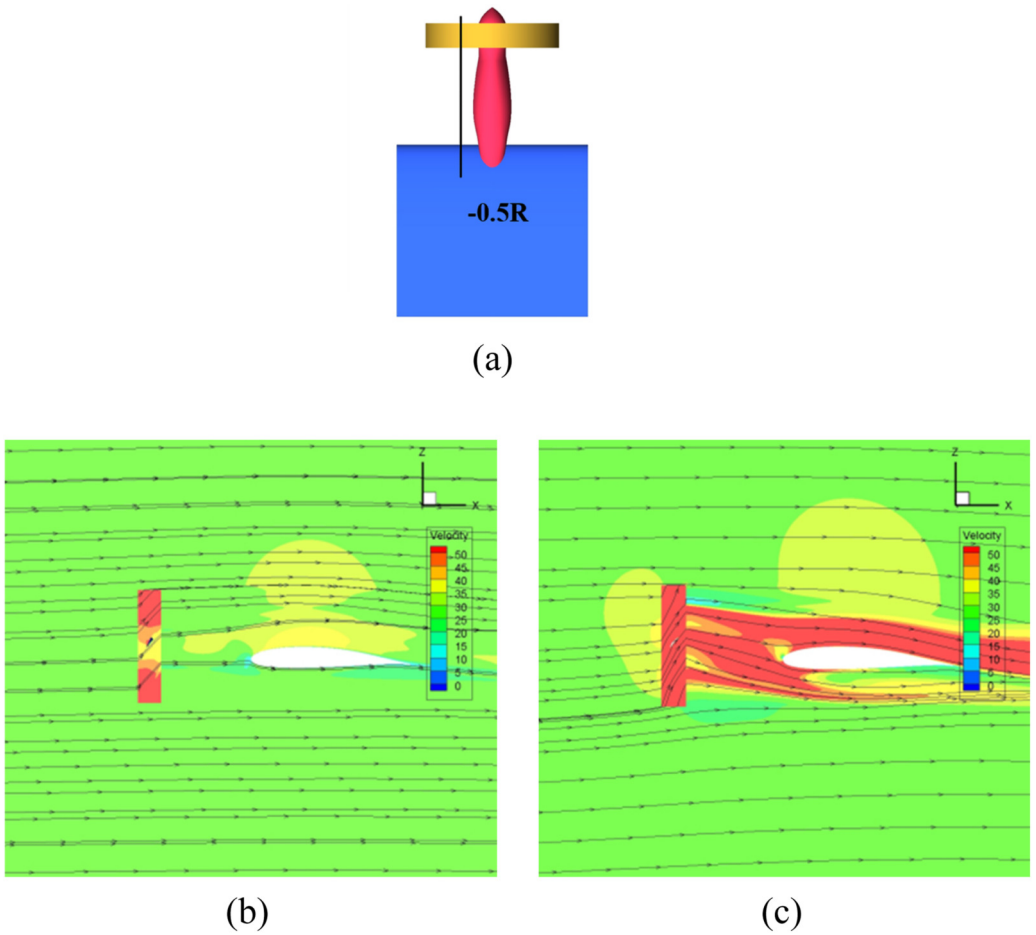

FIGURE 12 | Velocity contour map of a radius 285 propeller in the wing section (Y = −0.5R). **(a)** −0.5R station. **(b)** 2000 rpm **(c)** 5000 rpm.

Single Propeller Slipstream Effects

The effect of rotational speed on the aerodynamic characteristics was investigated for three propeller configurations to compare their slipstream impacts. **Figure 11** presents the lift and drag characteristics of the wing section for the three propeller types at different rotational speeds, under an inflow velocity of 28 m/s and an angle of attack of 0°.

In **Figure 11**, the slipstream effects of propellers with different radii (denoted as r285, r300, and r330) are compared. The resulting aerodynamic force coefficients of the wing segments under the propeller slipstream are represented by the ratio Cr.

Figure 11a shows that the influence of propeller slipstream on the wing-section lift coefficient exhibits a consistent trend with rotational speed for different propeller radii. Specifically, the lift coefficient decreases as the propeller radius increases. At any given speed, the configuration with the 285 mm radius propeller (CLr285) yields the highest lift coefficient. Conversely, for a fixed radius, the lift coefficient increases with rotational speed.

As shown in **Figure 11b**, the drag coefficient, however, exhibits a more complex dependence on radius. The drag coefficient, however, exhibits a more complex dependence on radius. The maximum drag coefficient occurs for the 285 mm propeller at 2000 rpm. As rotational speed increases, the drag coefficient for the 285 mm propeller (CDr285) decreases steadily. In contrast, the drag coefficients for the 300 mm (CDr300) and 330 mm (CDr330) propellers increase, with CDr300 demonstrating a steeper rate of increase than CDr330.

To further analyze the variation in the drag coefficient for the r285 case shown in **Figure 11**, the present study takes the 285 mm-radius propeller flow field as an example and selects the location at y = −0.5R for analysis, as illustrated in **Figure 12a**. The effects of the propeller slipstream on the drag characteristics are investigated at rotational speeds of 2000 and 5,000 rpm, with an inflow velocity of 28 m/s and an angle of attack of 0°.

As shown in **Figures 12b,c**, the slipstream downstream of the propeller becomes more concentrated at the y = −0.5R location. Meanwhile, the flow deflection effect is enhanced, with an obvious downward deflection that alters the flow from a horizontal state before impinging on the airfoil segment. The component of the aerodynamic force perpendicular to the wind-axis streamline is opposite to the component parallel to the chord direction. Consequently, the contributions to drag from these aerodynamic components partially cancel each other out.

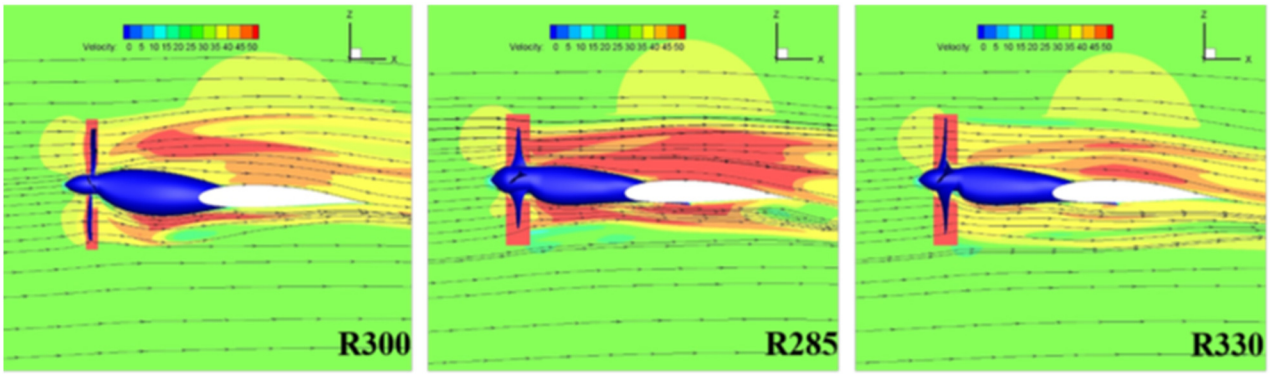

(a)

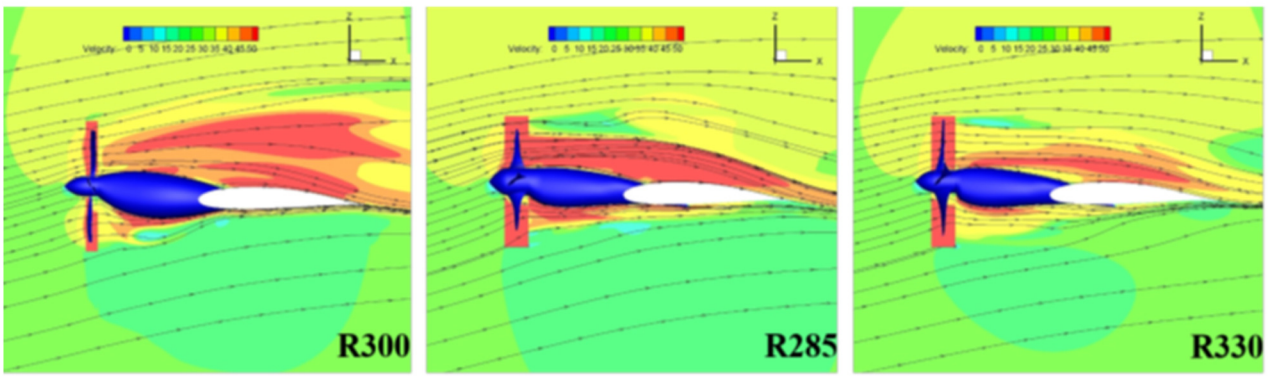

(b)

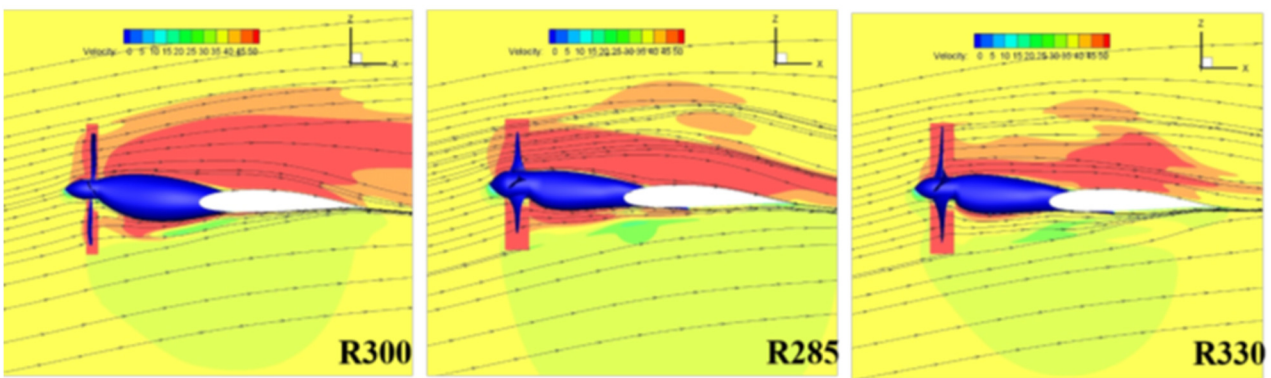

(c)

FIGURE 13 | Velocity contour map at different inflow velocities and angles of attack (4,500 rpm). **(a)** 28 m/s incoming flow, 0° angle of attack. **(b)** 28 m/s incoming flow, 8° angle of attack. **(c)** 38 m/s incoming flow, 8° angle of attack.

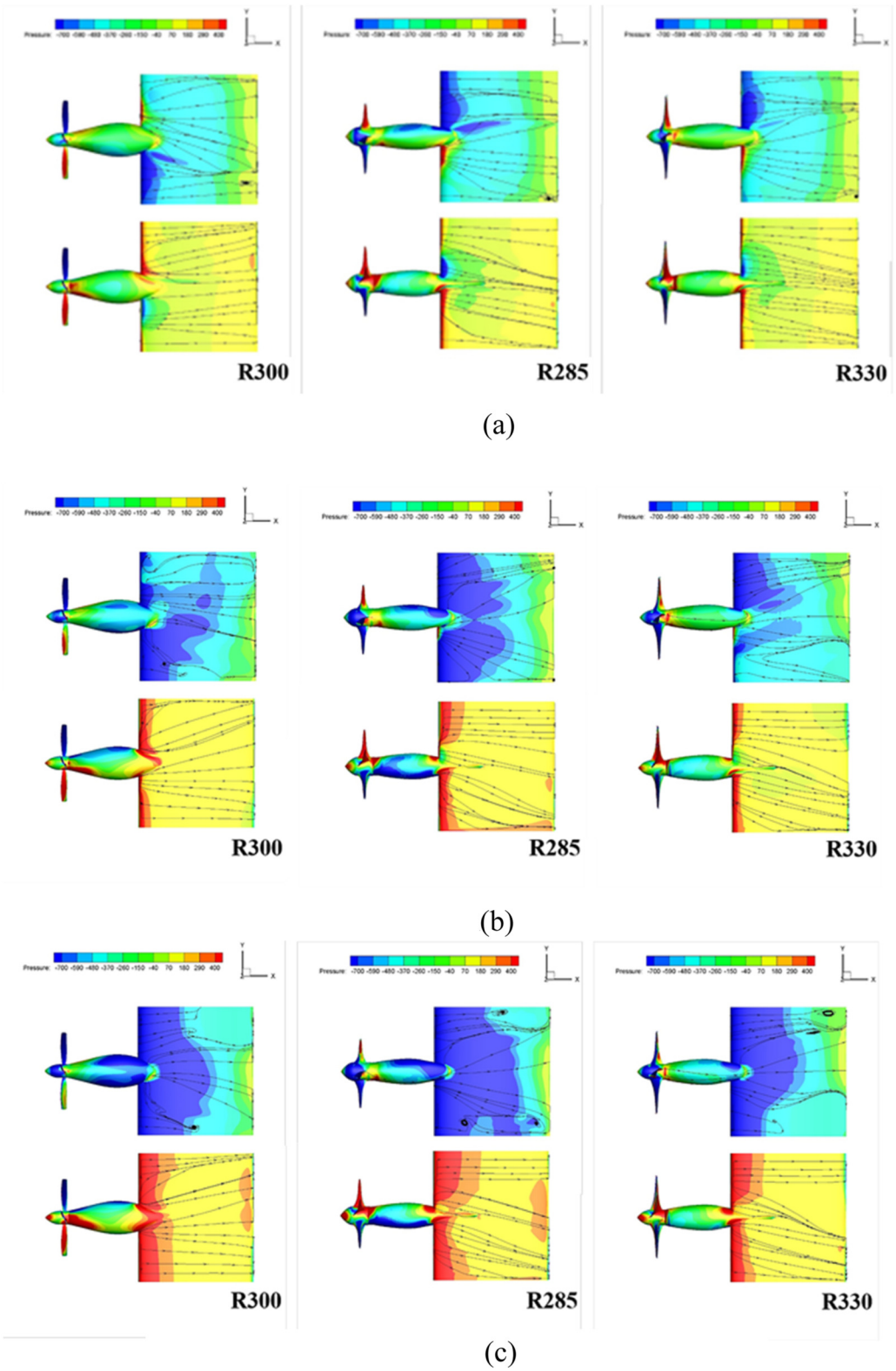

FIGURE 14 | Pressure cloud maps at different inflow velocities and angles of attack (4,500 rpm). **(a)** 28 m/s incoming flow, 0° angle of attack. **(b)** 28 m/s incoming flow, 8° angle of attack. **(c)** 38 m/s incoming flow, 8° angle of attack.

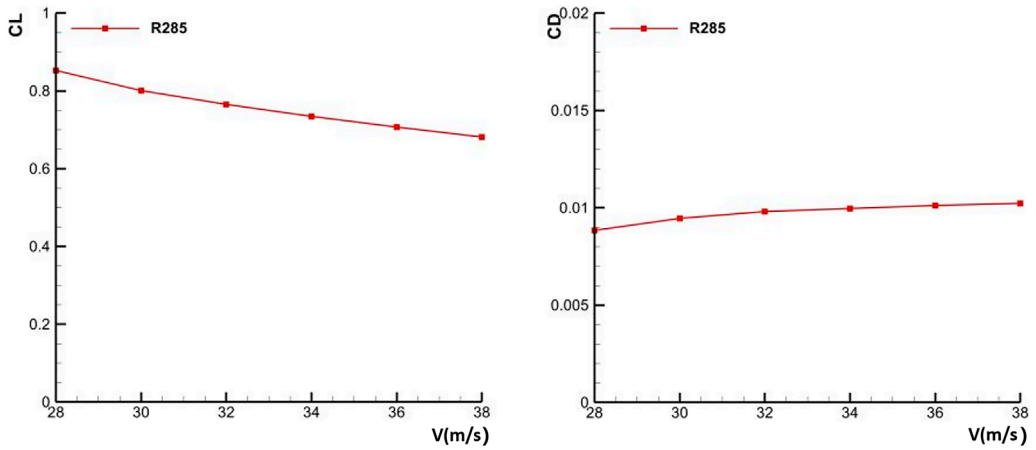

FIGURE 15 | Lift and drag coefficients of wing section at different incoming flow velocities.

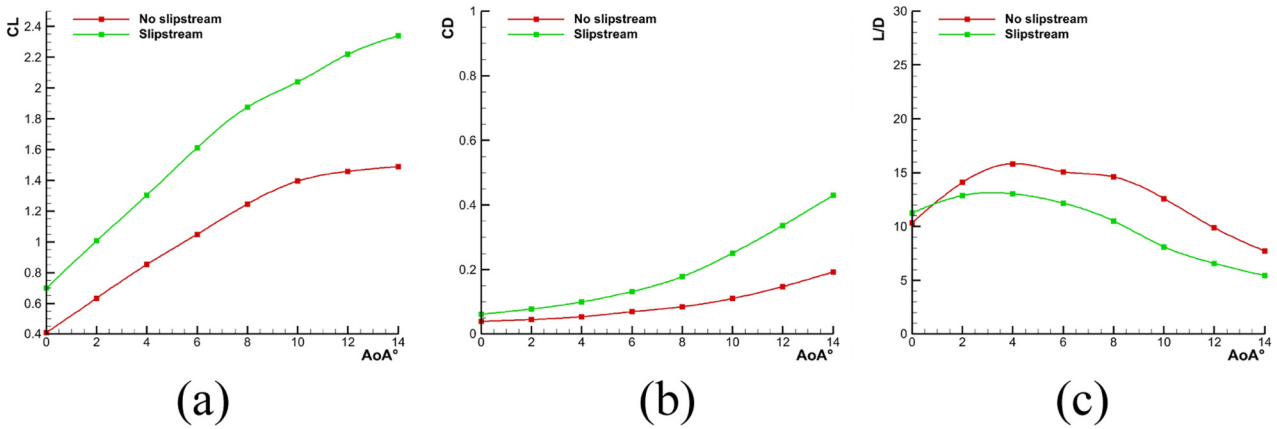

FIGURE 16 | Aerodynamic characteristics of the entire aircraft with and without slipstream conditions. **(a)** C_L. **(b)** C_D. **(c)** L/D.

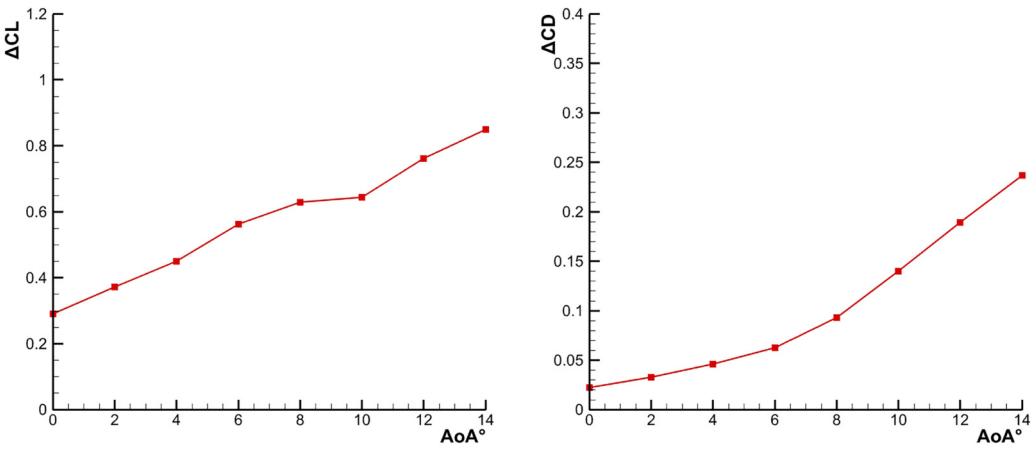

FIGURE 17 | Difference between the lift and drag coefficients with and without slip flow conditions.

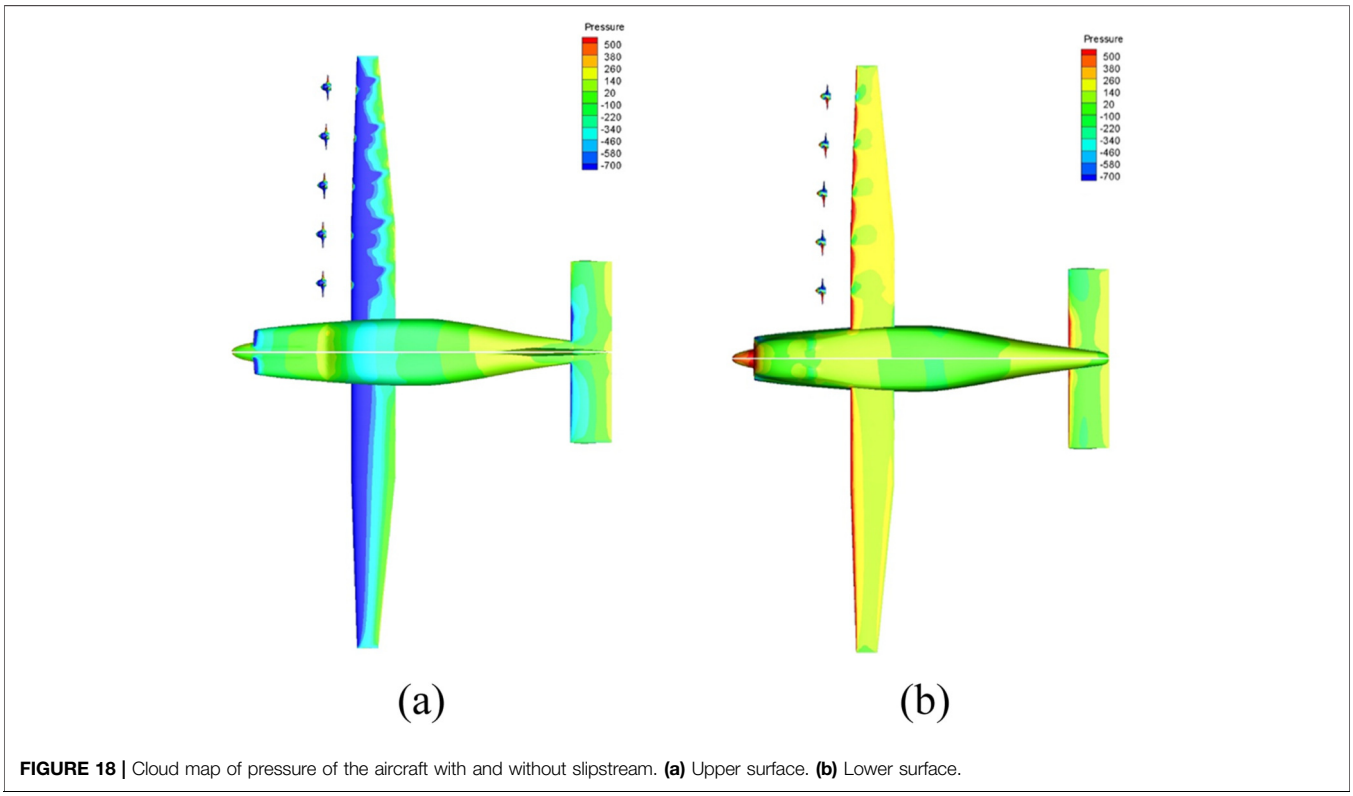

FIGURE 18 | Cloud map of pressure of the aircraft with and without slipstream. **(a)** Upper surface. **(b)** Lower surface.

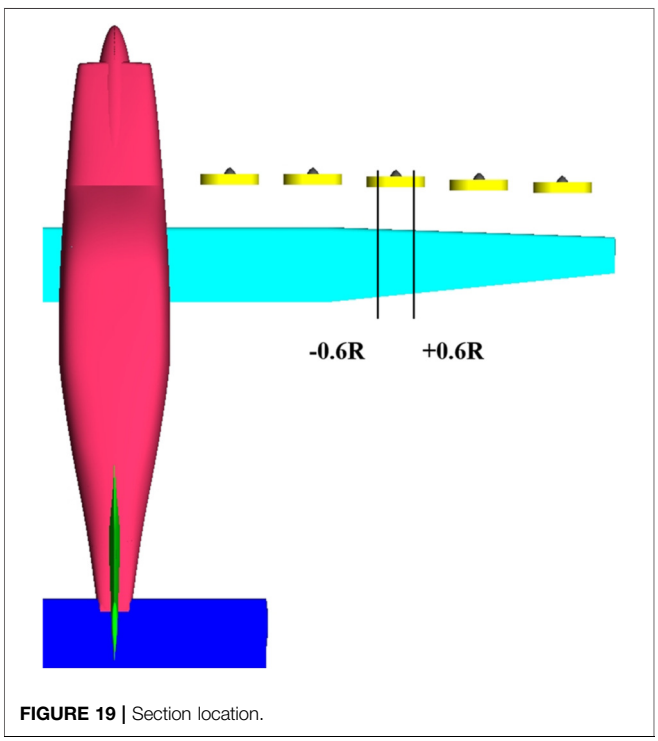

FIGURE 19 | Section location.

Furthermore, due to the velocity jump at the interface between the rotating and stationary domains arising from their differing velocity components, the analysis here focuses solely on the influence of the slipstream on the stationary domain, with the internal flow variations within the rotating domain not being discussed.

At the y = +0.5R location, the airflow deflects upward. A comprehensive comparison of the deflection magnitudes indicates that the downward deflection is stronger than the upward deflection. This mechanism leads to a gradual reduction in the drag coefficient with increasing rotational speed, which explains the flow characteristics presented in **Figure 11b**.

The flow field on the wing symmetry plane (y = 0) was analyzed to examine the effects of inflow velocity and angle of attack on the propeller slipstream. **Figure 13** presents the velocity contours of the slipstream field on the symmetry plane (y = 0) for propellers of different radii rotating at 4,500 rpm. The minimum drag coefficient (CDr330) occurs under the inflow conditions specified in **Figure 13a**. As shown in **Figure 13a**, this correlates with the strongest airflow deflection within the slipstream zone generated by the r330 propeller, whereas the deflection is weakest for the r285 propeller. Comparing **Figure 13a** with **Figure 13c** under identical inflow conditions reveals that a propeller with a smaller disc radius produces a stronger and more concentrated flow acceleration, yielding a more pronounced slipstream effect. Furthermore, a comparison between **Figures 13a,b** indicates that at a fixed inflow velocity, a smaller-radius propeller exerts a greater influence on redirecting the slipstream and enhancing its velocity as the angle of attack increases. A comparison of **Figures 13b,c** shows that the extent of the slipstream zone increases with inflow velocity. In contrast, the high-velocity region on the wing

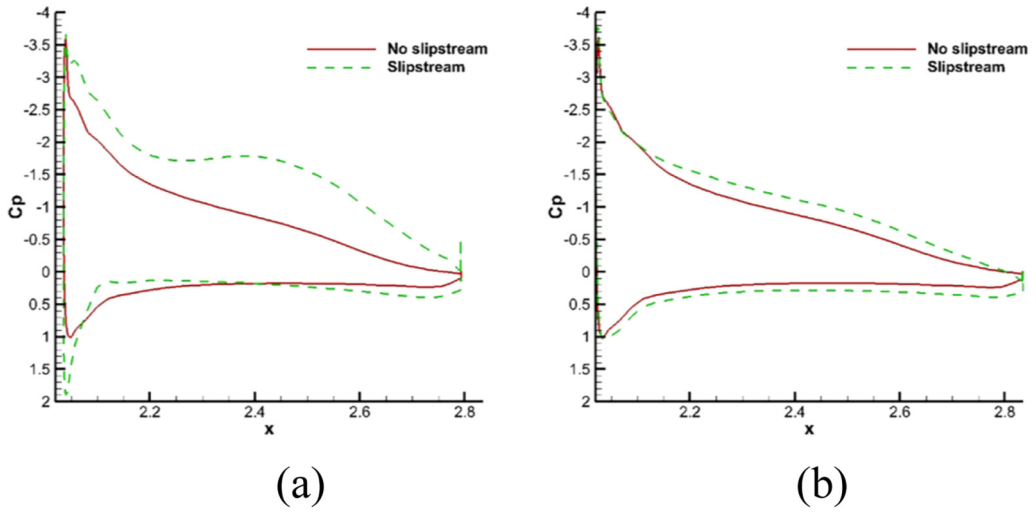

FIGURE 20 | Pressure coefficient distribution at ±0.6R position for wing with and without slipstream. **(a)** y = +0.6R. **(b)** y = −0.6R.

upper surface induced by the slipstream diminishes at 38 m/s compared to 28 m/s.

To further investigate the modifications in the slipstream-induced flow field, the surface pressure on the wing section was analyzed, with the results presented in **Figure 14**. **Figure 14** shows the pressure distribution on the upper wing surface for propellers of different radii at a rotational speed of 4,500 rpm.

Due to differences in blade design, the four-bladed r300 propeller induces a left-rotating airflow downstream. This rotation creates a low-pressure region on the rightwing section (as viewed from upstream). In contrast, as seen in **Figure 14a**, the five-bladed r285 and r300 propellers generate a low-pressure zone on the leftwing section due to the opposite sense of swirl imparted by the blade geometry.

As the angle of attack increases, the negative pressure zone on the wing surface expands, attributed to the enhanced impact of the high-speed slipstream (**Figures 14b,c**). Concurrently, at a fixed angle of attack, an increase in freestream velocity causes this low-pressure region to extend further upstream. However, the magnitude of the negative pressure peak is lower under high-speed conditions compared to low-speed conditions. This reduction in suction peak strength leads to a gradual decrease in the lift coefficient with increasing velocity.

As shown in **Figure 15**, according to the analysis of the lift and drag coefficients for the r285 propeller at different inflow velocities, the slipstream effect induced at a fixed rotational speed of 4500 rpm gradually weakens as the inflow velocity increases. Meanwhile, the inflow velocity itself is insufficient to strengthen the slipstream induction, resulting in a decrease in the lift coefficient of the wing segment. In addition, the drag coefficient increases gradually with rising inflow velocity.

It is clear that the propeller slipstream accelerates the flow along the axial direction, deflects the airflow direction, and increases the local inflow velocity. The static pressure changes abruptly across the propeller disk, which has a significant influence on the overall flow field over the wing. Furthermore, the overall aerodynamic characteristics are strongly affected by different propeller configurations, and can be altered by adjusting specific geometric or operational parameters.

Distributed Propeller Aircraft Aerodynamic Characteristics

The aerodynamic characteristics of the complete aircraft, including lift, drag, and lift-to-drag ratio (L/D), with and without propeller slipstream, are presented in **Figure 16** at the typical flow conditions of 8° angle of attack, 4,500 rpm, and 33 m/s freestream velocity.

Figure 16 shows that the lift coefficient increases linearly with angle of attack up to approximately 8°, both with and without slipstream. Beyond this point, the rate of increase diminishes due to progressive flow separation on the wing surface.

The application of propeller slipstream increases the lift-curve slope and extends the linear range of the lift coefficient compared to the clean configuration. Furthermore, it improves the stall characteristics and increases the stall angle of attack.

Near an 8° angle of attack—relevant for takeoff and landing—the slipstream augments the lift coefficient by more than 50%. This demonstrates that a propeller positioned to energize the flow over the wing can effectively enhance lift during low-speed flight phases.

However, the slipstream also increases the drag coefficient. At 8° angle of attack, the drag is nearly double that of the non-slipstream condition. Consequently, the lift-to-drag ratio is lower across most angles of attack when the slipstream is present, except at 0° angle of attack where a slight improvement is observed.

A comprehensive analysis of the aerodynamic characteristics reveals that, in the presence of slipstream, both lift and drag are increased compared to the clean (no-slipstream) configuration.

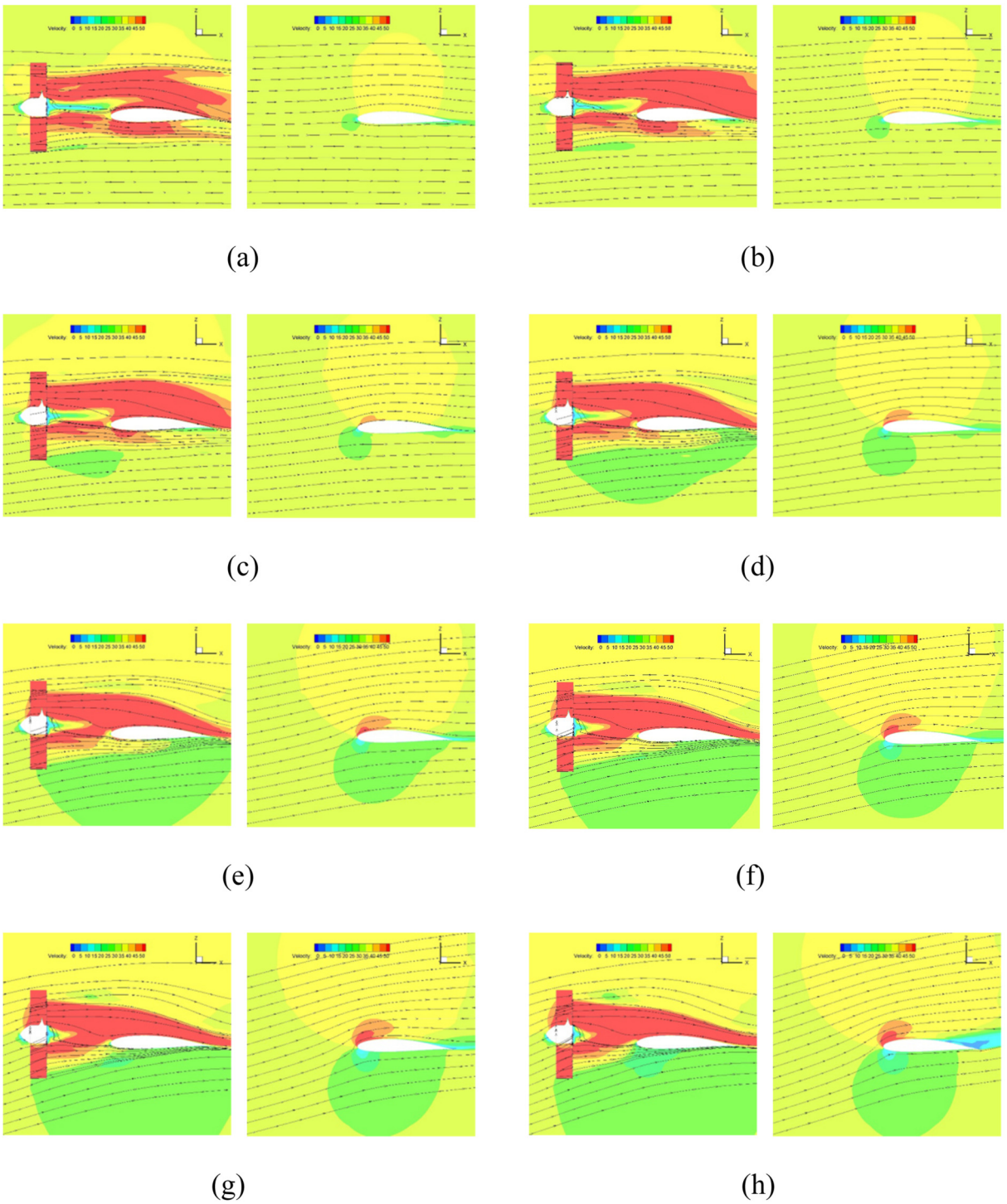

FIGURE 21 | Velocity cloud map with and without slipstream at different angles of attack. **(a)** 0°. **(b)** 2°. **(c)** 4°. **(d)** 6°. **(e)** 8°. **(f)** 10°. **(g)** 12°. **(h)** 14°.

However, the incremental gain in drag outweighs the gain in lift, leading to an overall reduction in the aircraft's lift-to-drag ratio.

The differentials in lift and drag coefficients between the slipstream and clean configurations are plotted in **Figure 17**, elucidating the impact of slipstream on aerodynamic performance. Both differentials exhibit a growing trend with increasing angle of attack. Notably, within an angle of attack of 6°, the lift differential rises significantly, whereas the drag

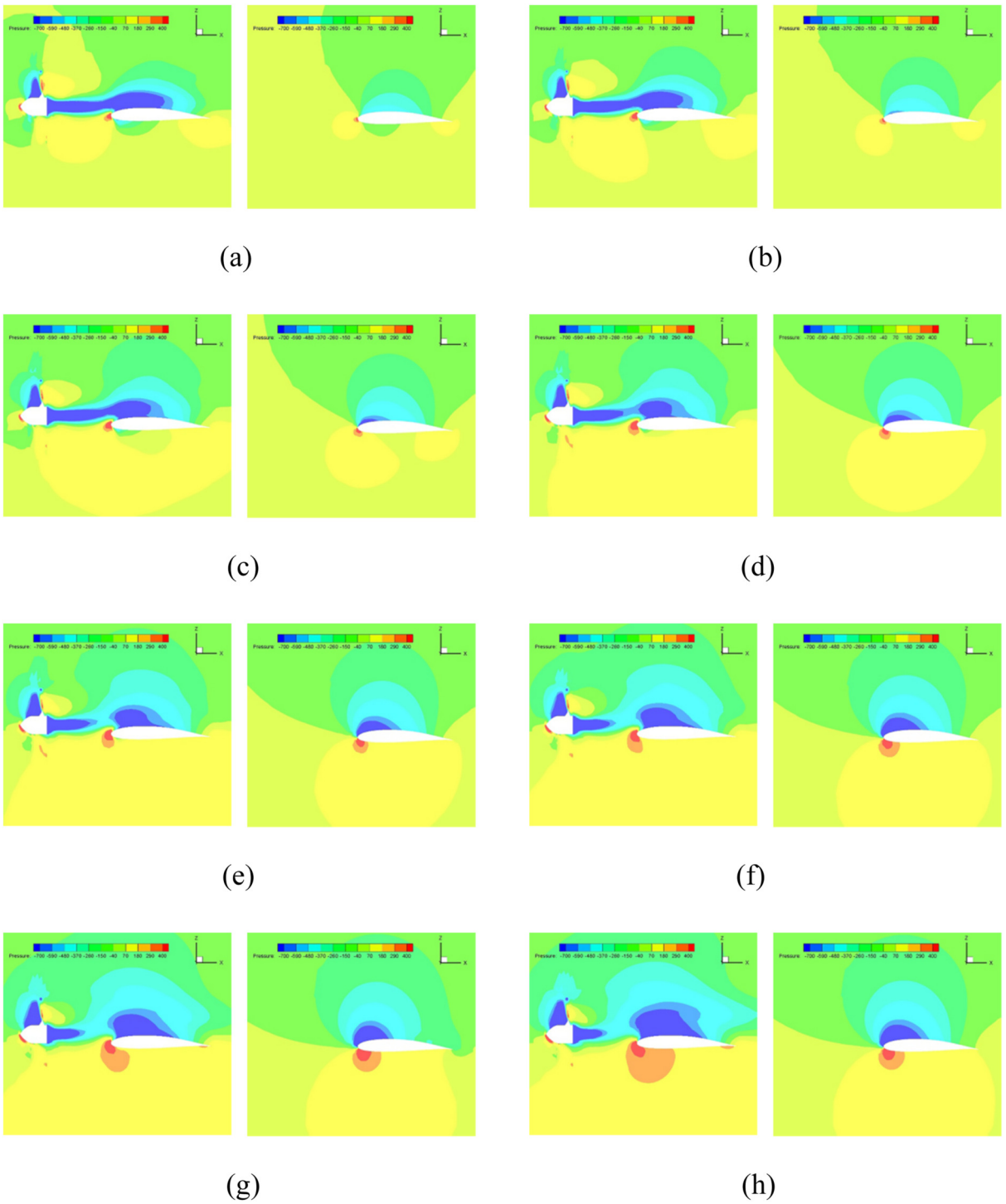

FIGURE 22 | Pressure cloud map with and without slipstream at different angles of attack. **(a)** 0°. **(b)** 2°. **(c)** 4°. **(d)** 6°. **(e)** 8°. **(f)** 10°. **(g)** 12°. **(h)** 14°.

differential shows no marked increase. This behavior may be attributed to the slipstream's influence on the local flow: the propeller partially alters the direction of the incoming airflow ahead of the wing, resulting in a slight reduction in the effective angle of attack for wing sections within the slipstream. Concurrently, the energy imparted by the slipstream to the wing's boundary layer mitigates the drag rise typically associated with flow separation.

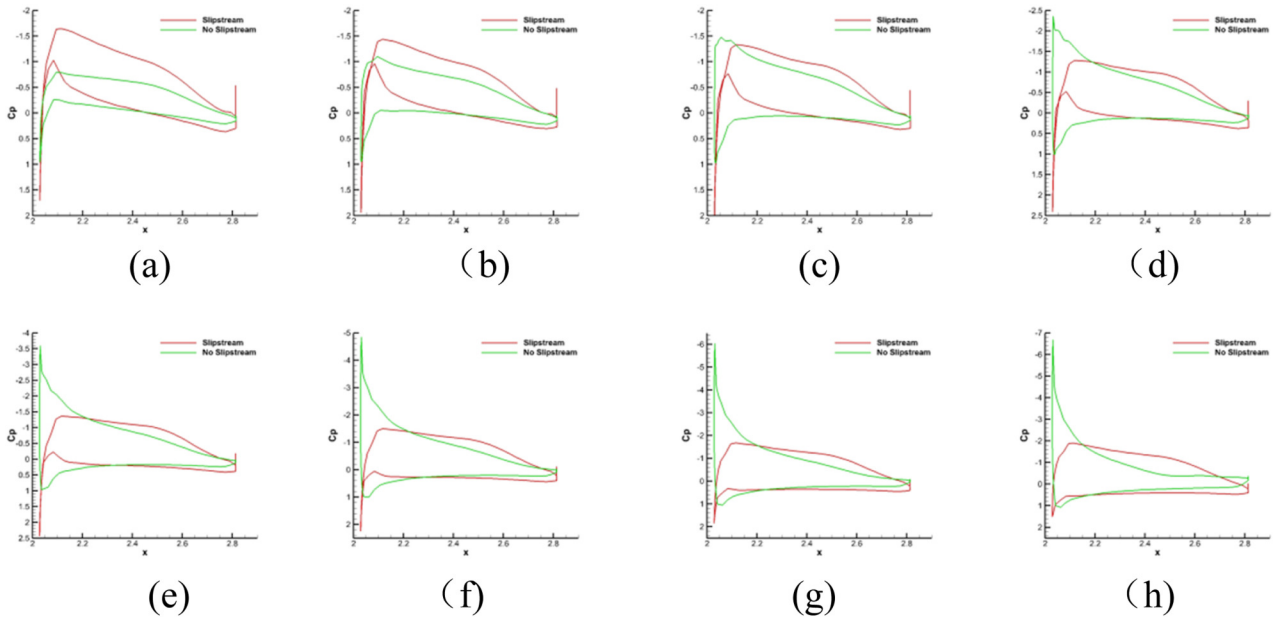

FIGURE 23 | Pressure distribution at y = 3.373 m at different angles of attack with and without slipstream. **(a)** 0°. **(b)** 2°. **(c)** 4°. **(d)** 6°. **(e)** 8°. **(f)** 10°. **(g)** 12°. **(h)** 14°.

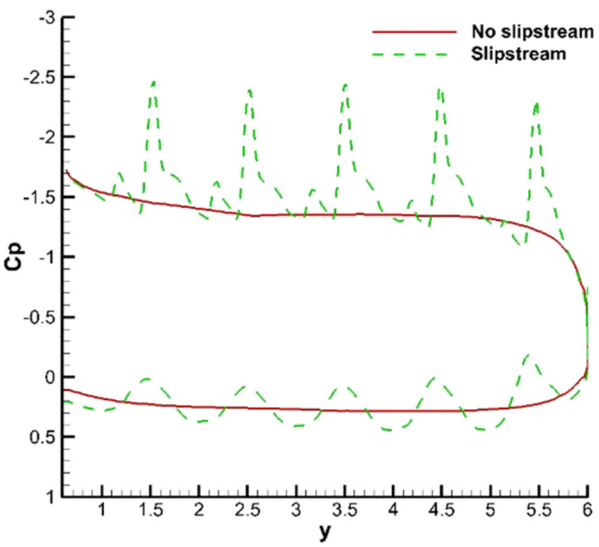

FIGURE 24 | Pressure coefficient distribution along the wing spanwise direction with and without propeller slipstream.

Wing Pressure Distribution

At a propeller rotational speed of 4,500 rpm, an angle of attack of 8°, and an inflow velocity of 33 m/s, the pressure contours on the upper and lower surfaces of the full aircraft with and without slipstream effects are presented in **Figure 18**.

The rotation of the propeller accelerates the incoming flow, leading to an increase in the static pressure ahead of the wing. In the slipstream case, the low-pressure region on the upper wing surface is mainly distributed downstream of the propeller. Viewed along the flow direction, the wing leading-edge propeller rotates clockwise, inducing upward flow deflection on the inner side and downward deflection on the outer side of the slipstream.

Combined, these effects make the low-pressure region on the wing more intense and extensive compared with the no-slipstream condition. Behind a single propeller, the low-pressure region on the wing tip side is larger than that on the fuselage side.

In the slipstream case, the high-pressure region on the upper wing surface is also mainly located downstream of the propeller. On the wing leading edge behind a single propeller, the high-pressure zone on the tip side is larger than that on the fuselage side. For the lower wing surface, the high-pressure region becomes more intense and extensive when the slipstream effect is present.

To examine the effects of a single propeller's slipstream on the wing in detail, Propeller No. 3 was selected for analysis. The pressure distributions on the wing at spanwise positions of ±0.6R from the propeller axis were compared, and the locations of these wing sections are illustrated in **Figure 19**. Finally, the pressure coefficient distributions over the wing sections at ±0.6R, with and without propeller slipstream, are presented in **Figure 20**.

Analysis of the pressure distributions in **Figure 20** indicates distinct differences between the slipstream and clean-configuration cases. At the +0.6R station, the wing section exhibits higher suction under slipstream conditions. While the suction peak locations are nearly coincident, the leading-edge lower-surface pressure peak is more pronounced with the slipstream.

Conversely, at the −0.6R station, the leading-edge suction with slipstream is greater, but the associated suction peak magnitude is smaller compared to the clean configuration.

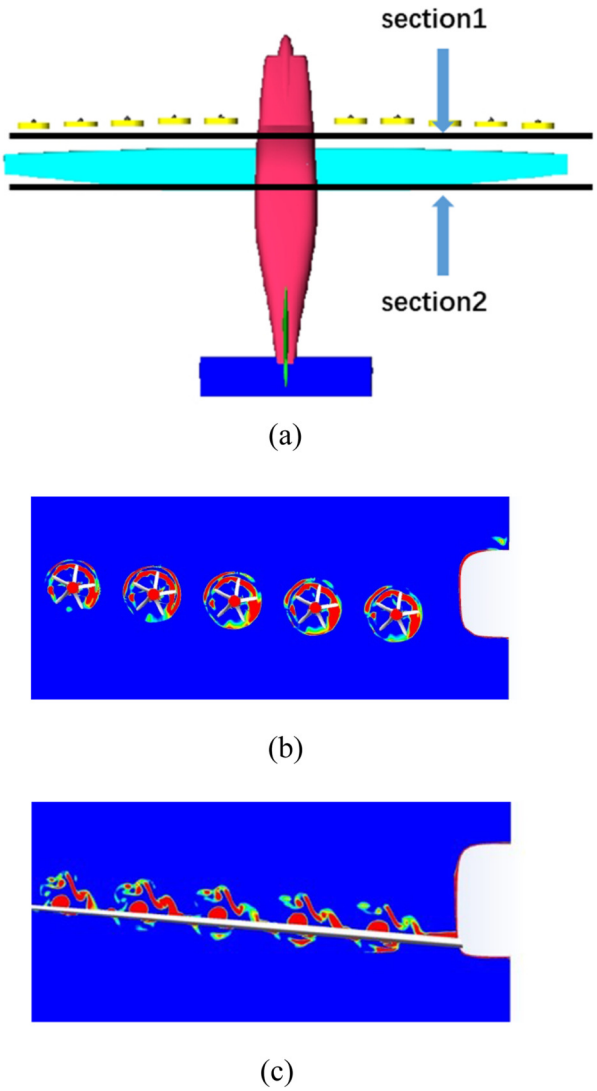

FIGURE 25 | Vortices distribution on the wing section. **(a)** Locations of the sections used for analysis. **(b)** Section 1 vortices distribution. **(c)** Section 2 vortices distribution.

The leading-edge lower-surface pressure is also higher in the presence of slipstream.

Despite the significant asymmetry in pressure distribution across the propeller axis, both sides contribute positively to the total lift generation.

Typical Flow Field of the Aircraft

Consistent with the previous section, Propeller No. 3 is still selected as the analysis object. The focus is placed on the flow phenomena reflected in the wing pressure and velocity contours, with and without the propeller slipstream effect (4,500 rpm), over the angle of attack range of 0°–14°.

Streamlines and pressure contours of the wing at the spanwise location y = 3.373 m (on the axis of the No. 3 propeller) are presented in **Figures 21**, **22** for both slipstream and no-slipstream cases. When the slipstream is present, the flow velocity downstream of the propeller is higher than in the no-slipstream case, and the deflection of the high-speed region is less pronounced with variations in the angle of attack. At low angles of attack, the propeller blades induce an upwash that deflects the slipstream below the wing toward the upper surface as the angle of attack increases.

As shown in **Figure 22**, the low-pressure region between the propeller and the wing is disrupted by the upwash flow with increasing angle of attack, which delays the suction peak and leads to a lower flow velocity near the leading edge compared with the clean wing configuration.

The pressure distribution along the wing chord at the spanwise station y = 3.373 m is shown in **Figure 23**. These data were obtained at a freestream velocity of 33 m/s and a propeller speed of 4,500 rpm, with increasing angle of attack.

The pressure distribution over the wing section is altered by the propeller slipstream. The downwash component decreases the local angle of attack, while the upwash component increases it. At low angles of attack, the suction peak near the leading edge is higher with slipstream than without it. As the angle of attack increases, this peak diminishes in the presence of slipstream because the propeller-induced flow washes over the leading edge, disrupting the local airflow. In contrast, without slipstream, the suction peak generally increases with angle of attack due to the accelerating flow over the leading edge.

On the pressure surface (lower surface), the peak pressure exhibits a consistent trend in both configurations, gradually becoming less negative (or more positive) with increasing angle of attack. However, due to the higher induced velocity, the pressure magnitudes on the wing are generally greater with slipstream than without it.

Figure 24 presents a comparison of the spanwise pressure distribution at a wing section located at x = 2.2m, under an 8° angle of attack with clockwise blade rotation, for conditions with and without slipstream.

In the absence of slipstream, the pressure distribution on the wing's lower surface follows a regular pattern. With slipstream, however, the suction (negative pressure) on the upper surface is enhanced at most spanwise locations compared to the clean configuration.

A distinct pressure modulation induced by the propeller blades is evident. On the left side of the propeller axis, the slipstream generates five localized suction peaks on the upper surface, each corresponding to a region of lower pressure compared to the non-slipstream case. Concurrently, five distinct high-pressure zones appear on the lower surface.

Wing Interference Effects on the Propeller Slipstream

Figure 25 presents the rotational vortex structures at different spanwise sections along the wing. Section 1 is located downstream of the propeller and upstream of the wing leading edge, while Section 2 is positioned near the wing trailing edge. **Figure 25b** shows the rotational vortex field in the region downstream of the propeller and upstream of the wing. Prior

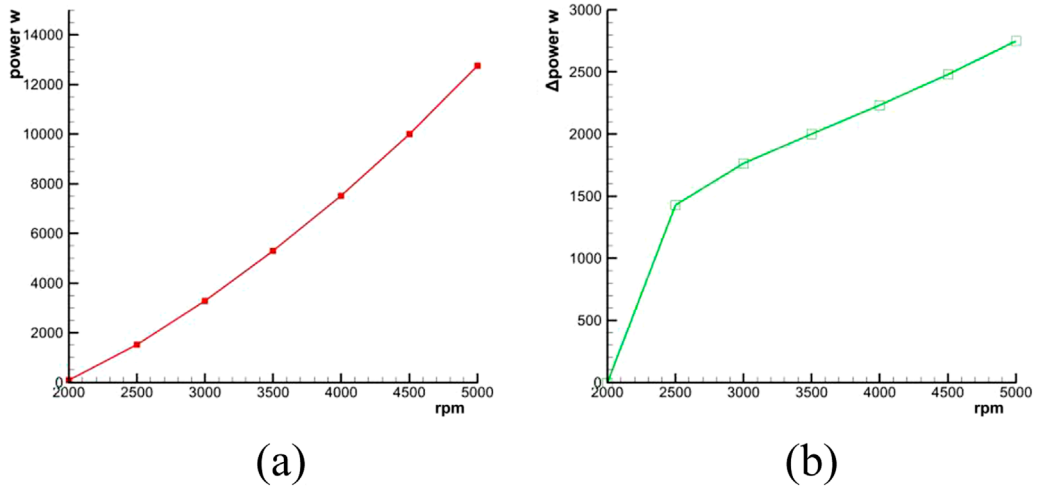

FIGURE 26 | Variation of power with rotational speed. **(a)** Power. **(b)** ΔPower.

to interaction with the wing, the extent of the vortex field approximates the propeller disk area, retaining a relatively complete structure. However, at the wing trailing edge (**Figure 25c**), the vortex structure is no longer intact. The presence of the wing significantly disrupts the vortex, which develops in the spanwise direction at this location, thus exerting a considerable influence on the pressure distribution over the wing.

Power Consumption Versus Rotational Speed

The power required by the propeller increases with its rotational speed. The measured relationship between power and speed is presented in **Figure 26**. The power for each propeller was measured individually, and the average value was used to represent the power at each rotational speed in the plot.

As shown in **Figure 26**, power consumption is relatively low at low rotational speeds, measuring below 100 W at 2000 rpm. The power then increases approximately parabolically with speed, reaching its maximum at 5,000 rpm.

This rapid increase in power demand poses a challenge for the nacelle motor design. The operational speed range of the propeller is ultimately limited by the maximum power output of the motor. Furthermore, at very high rotational speeds, propeller tip effects may become significant and require additional consideration in the aerodynamic design.

CONCLUSION

This study investigated the influence of key design parameters on the slipstream and associated aerodynamic mechanisms of a distributed propeller aircraft configuration. Using the MRF method for quasi-steady simulations, the aerodynamic characteristics of various propeller designs were analyzed. The main conclusions are as follows:

1. The design of the propeller configuration is intrinsically linked to the effective induced slipstream field. The slipstream significantly accelerates the flow downstream of the propeller disk, with further acceleration due to wing interaction and streamtube contraction. However, different propeller geometries lead to distinct aerodynamic outcomes. While the lift coefficient increases with rotational speed, the drag coefficient exhibits disparate trends depending on the configuration. Therefore, propeller configuration design should be finalized prior to the detailed design of the full distributed propulsion aircraft.
2. Compared to the clean (no-slipstream) configuration, the presence of slipstream increases both lift and drag, but results in a lower overall lift-to-drag ratio. The slipstream induces asymmetric changes in the effective local angle of attack on either side of the propeller axis, altering the spanwise lift distribution and vorticity field. As the propeller tip vortex interacts with the wing, it splits into upper and lower segments, generating a lateral secondary flow around the wing. The presence of the wing, in turn, modifies the structure and development of vortices within the slipstream.
3. The rotational speed of the propeller exerts a notable influence on the overall pressure distribution over the wing. The required power exhibits a rapid increasing trend with rotational speed, which imposes significant demands on motor design and system integration. To further optimize the aerodynamic performance of this configuration, future investigations could explore a wider range of propeller geometries and conduct parametric analyses focusing on rotational speed and direction.

Additionally, incorporating performance metrics such as thrust and propulsive efficiency into the optimization process would be beneficial for refining the distributed propulsion layout.

DATA AVAILABILITY STATEMENT

The original contributions presented in the study are included in the article/supplementary material, further inquiries can be directed to the corresponding author.

AUTHOR CONTRIBUTIONS

ZL: Conceptualization, Validation, Formal analysis, Visualization, Writing; MZ: Methodology, Investigation and polishing; YX: Project administration; YW: Validation, editing. HZ: Methodology. YL: Funding acquisition, Supervision. All authors contributed to the article and approved the submitted version.

FUNDING

The author(s) declared that financial support was not received for this work and/or its publication.

CONFLICT OF INTEREST

The author(s) declared that this work was conducted in the absence of any commercial or financial relationships that could be construed as a potential conflict of interest.

GENERATIVE AI STATEMENT

The author(s) declared that generative AI was not used in the creation of this manuscript.

Any alternative text (alt text) provided alongside figures in this article has been generated by Frontiers with the support of artificial intelligence and reasonable efforts have been made to ensure accuracy, including review by the authors wherever possible. If you identify any issues, please contact us.

REFERENCES

1. Guo Y. Outline for the Development of Green Aviation Manufacturing Industry. *China Industry News* (2023) 10–27. (005).
2. Mrazova M. Sustainable Development–the Key for Green Aviation. *Incas Bull* (2014) 6(1):109–22. doi:10.13111/2066-8201.2014.6.1.10
3. Xue DB, Chen XM, Yu SW. Sustainable Aviation for a Greener Future. *Commun Earth Environ* (2025) 6:233. doi:10.1038/s43247-025-02222-3
4. Sarkar AN. Evolving Green Aviation Transport System: A Hoilistic Approah to Sustainable Green Market Development. *Am J Clim Change* (2012) 1(3): 164–80. doi:10.4236/ajcc.2012.13014
5. Huang J, Yang FT. Development and Challenges of Electric Aircraft with New Energies. *Acta Aeronautica Et Astronautica Sinica* (2016) 37(1):57–68.
6. Gohardani AS, Doulgeris G, Singh R. Challenges of Future Aircraft Propulsion: A Review of Distributed Propulsion Technology and Its Potential Application for the All Electric Commercial Aircraft. *Prog Aerospace Sci* (2011) 47(5): 369–91. doi:10.1016/j.paerosci.2010.09.001
7. Kong XH, Zhang ZR, Lu JW, Li JC, Yu L. Review of Electric Power System of Distributed Electric Propulsion Aircraft. *Acta Aeronautica et Astronautica Sinica* (2018) 39(1):46–62.
8. Huang J. Survey on Design Technology of Distributed Electric Propulsion Aircraft. *Acta Aeronautica Et Astronautica Sinica* (2021) 042(003):7–23.
9. Patterson MD, German B. Conceptual Design of Electric Aircraft with Distributed Propellers: Multidisciplinary Analysis Needs and Aerodynamic Modeling Development. *52nd Aerospace Sci Meet* (2014). doi:10.2514/6.2014-0534
10. Moore MD, Fredericks B. Misconceptions of Electric Aircraft and Their Emergent Aviation Markets. *52nd Aerospace Sci Meet* (2014). doi:10.2514/6. 2014-0535
11. Xu DK. NASA Restructures Aeronautic Research Programs. *Int Aviation* (2015)(3) 69–71.
12. Murphy PC, Landman D. Experiment Design for Complex VTOL Aircraft with Distributed Propulsion and Tilt Wing. In: *AIAA Atmospheric Flight Mechanics Conference AIAA* (2015). doi:10.2514/6.2015-0017
13. Keller D. Towards Higher Aerodynamic Efficiency of Propeller-Driven Aircraft with Distributed Propulsion. *CEAS Aeronaut J* (2021) 12:777–91. doi:10.1007/s13272-021-00535-5
14. Wang HB, Zhu XP, Zhou Z, Xu XP. Aerodynamic Investigation on Propeller Slipstream Flows for Solar Powered Airplanes. *J Northwest Polytechnical Univ* (2015) 33(6):913–20.
15. Christie R, Dubois A, Derlaga JM. *Cooling of Electric Motors Used for Propulsion on SCEPTOR:NASA- TM-2017-219134* (2017).
16. Patterson MD, Derlaga JM, Borer NK. High-Lift Propeller System Configuration Selection for Nasa's SCEPTOR Distributed Electric Propulsion Flight Demonstrator. *16th AIAA Aviation Technol AIAA* (2016). doi:10.2514/6.2016-3922
17. Busan RC, Rothhaar PM, Croom MA, Murphy PC, Grafton SB, O-Neal AW. Enabling Advanced Wind-Tunnel Research Methods Using the NASA Langley 12-Foot Low Speed Tunnel. *AIAA Aviation and Aeronautics Forum and Exposition* (2014). doi:10.2514/6.2014-3000
18. William JF, Mark DM, Ronald CB. Benefits of Hybrid-Electric Propulsion to Achieve 4x Increase in Cruise Efficiency for a VTOL Aircraft. In: *AIAA Aviation 2013International Powered Lift Conference* (2013). doi:10.2514/6. 2013-4324
19. Rothhaar PM, Murphy PC, Bacon BJ, Gregory IM, Grauer JA, Busan RC, et al. NASA Langley Distributed Propulsion VTOL Tilt Wing Aircraft Testing, Modeling, Simulation, Control, and Flight Test Development. In: *AIAA AFM Conference* (2014). doi:10.2514/6.2014-2999
20. Patterson MD, Borern NK. Approach Considerations in Aircraft with High-Lift Propeller Systems. In: *17th AIAA Aviation Technology, Integration, and Operations Conference* (2017). doi:10.2514/6.2017-3782
21. Litherland BL, Patterson MD, Derlaga JM, Borer NK. *A Method for Designing Conforming Folding Propellers AIAA* (2017). p. 3781. doi:10.2514/6.2017-3781
22. Stoll AM, Bevirt JB, Moore MD, Fredericks WJ, Borer NK. Drag Reduction Through Distributed Electric Propulsion. In: *14th AIAA Aviation Technology, Integration, and Operations Conference* (2014). doi:10.2514/6.2014-2851
23. Stoll AM, Mikic GV. Design Studies of Thin-Haul Commuter Aircraft with Distributed Electric Propulsion. In: *16th AIAA Aviation Technology, Integration, and Operations Conference* (2016). doi:10.2514/6.2016-3765
24. Patterson MD, German B. Wing Aerodynamic Analysis Incorporating One-Way Interaction with Distributed Propellers. In: *Proceedings of the 14th AIAA Aviation Technology, Integration, and Operations Conference* (2014). doi:10. 2514/6.2014-2852
25. Pavel H, Jan K, Nikola Ž. Wing and Propeller Aerodynamic Interaction Through Nonlinear Lifting Line Theory and Blade Element Momentum Theory. *MATEC Web Conf.* (2018) 233: 00027. doi:10.1051/matecconf/ 201823300027
26. Marcus EA, Vries RD, Kulkarni AR, Veldhuis LL. Aerodynamic Investigation of an Over-the-Wing Propeller for Distributed Propulsion. In: *Proceedings of the 2018 AIAA Aerospace Sciences Meeting* (2018). doi:10.2514/6.2018-2053

27. Bohari B, Bronz M, Benard E, Borlon Q. Conceptual Design of Distributed Propeller Aircraft: Linear Aerodynamic Model Verification of Propeller-Wing Interaction. In: *Proceeding of the 7th European Conference for Aeronautica and Space Sciences* (2017). doi:10.13009/EUCASS2017-445
28. Bohari B, Borlon Q, Mendoza-santos PB, Sgueglia A, Benard E, Bronz M, et al. Conceptual Design of Distributed Propellers Aircraft: Non-Linear Aerodynamic Model Verification of Propeller-Wing Interaction in High-Lifting Configuration. In: *Proceedings of the 2018 AIAA Aerospace Sciences Meeting* (2018). doi:10.2514/6.2018-1742
29. Yang XC, Wang YT, Meng DH, Miao T, Wang W. Study on Wing Slipstream Effects of Distributed Propellers with Different Rotating Directions. *Acta Aerodynamica Sinica* (2019) 37(1):89–98.
30. Yang XC, Li W, Wang YT, Wang H, Yue H, Huang JT. Research on Aerodynamic Shape Design Scheme of a Distributed Propeller Transport Aircraft and Its Slipstream Effect. *J Northwest Polytechnical Univ* (2019) 37(2):361–8. doi:10.1051/jnwpu/20193720361
31. Yang W, Fan ZL, Wu WH, Yu L. Optimal Design of Distributed Propeller Layout Considering Slipstream Effect. *Acta Aerodynamica Sinica* (2021) 39(3):71–9.
32. Wang KL, Zhu XP, Zhou Z, Wang HB. Distributed Electric Propulsion Slipstream Aerodynamic Effects at Low Reynolds Number. *Acta Aeronautica et Astronautica Sinica* (2016) 37(9):2669–78.
33. Du Y, Liu Z, Shen M, Wu J, Zhang K, Jiang C, et al. An Efficient Parametric Modeling, Evaluation and Optimization Strategy for Aerodynamic Configuration Design of Evtol Aircraft. *Aerosp Res Commun* (2025) 3: 14986. doi:10.3389/arc.2025.14986
34. Ribeiro André FP, Ferreira C, Casalino D. On the Use of Filament-Based Free Wake Panel Methods for Preliminary Design of Propeller-Wing Configurations. *Aerospace Sci Technol* (2024) 144:108775. doi:10.1016/j.ast.2023.108775
35. Cao M, Liu K, Wang C, Wei J, Qin Z. Research on the Distributed Propeller Slipstream Effect of UAV Wing Based on the Actuator Disk Method. *Drones* (2023) 7(9):566. doi:10.3390/drones7090566
36. Chen GQ, Bai P, Chen BY, Li PF, Bai P, Ji CQ. Numerical Simulation Study on Propeller Slipstream Effect on High Altitude Long Endurance Unmanned Air Vehicle. *Proced Eng* (2015) 99:361–7. doi:10.1016/j.proeng.2014.12.548
37. Gerrit-Daniel S, Luis SF, Jared CD, Jeffrey AH, Gaetan KK, Cetin CK. Validation of Actuator Disk, Actuator Line and Sliding Mesh Methods Within the LAVA Solver. In: *Eleventh International Conference on Computational Fluid Dynamics (ICCFD11)* (2022). ICCFD11-2022-0903.
38. Yang AM, Liu JH, Weng PF. Navier-Stokes Computation About a Helicopter Rotor in Hover Using Chimera Grids and Multi-Grid Acceleration. *Acta Aerodynamica Sinica* (2009) 27(1):6–10.
39. Caradonna FX, Tung C. Experimental and Analytical Studies of a Model Helicopter Rotor in Hover. *Vertica* (1981) 5(2):149–61. doi:10.1016/0376-0421(81)90002-6